PERGAMON

Journal of Structural Geology 23 (2001) 1865–1881

JOURNAL OF STRUCTURAL GEOLOGY

www.elsevier.com/locate/jstrugeo

Fold mechanisms in the Canton Schist: constraints on the contribution of flexural flow

Aaron Stallard*, Ken Hickey[1]

School of Earth Sciences, James Cook University, Townsville 4811, Australia

Received 15 August 2000; revised 26 December 2000; accepted 31 January 2001

Abstract

Fold mechanisms operating in the Canton Schist have been resolved using the geometric relationship between folds and spiral inclusion trail geometries. Of the four end-member fold mechanisms, tangential–longitudinal strain folding and slip folding are unable to produce the observed inclusion trail and fold geometries, but a combination of flexural flow and pure shear folding is consistent with the geometric constraints. The maximum flexural flow component during each fold event was determined from the geometric data. During F_3 and F_4, flexural flow produced $\leq$27% and $\leq$37% of measured limb rotation, respectively, which corresponds to a maximum of 24° limb rotation by flexural flow in each fold event. To satisfy the geometric constraints, the remainder of limb rotation must be a product of pure shear folding. The maximum possible component of flexural flow folding during F_3 and F_4 increases with increased variation in vorticity between layers in the rock mass. In the flexural flow–pure shear model, a maximum of 28% of inclusion trail curvature is produced by rotation of porphyroblasts relative to (irrotational) fold limbs, with a minimum 72% curvature due to rotation of fold limbs relative to (irrotational) porphyroblasts. All model solutions produce less than $\approx 8°$ syn-folding porphyroblast rotation relative to geographic coordinates. © 2001 Elsevier Science Ltd. All rights reserved.

Keywords: Folding; Flexural flow; Inclusion trails; Porphyroblasts; Pure shear

1. Introduction

Folding of natural rocks is generally described in terms of four simple kinematic end-member models. They are tangential–longitudinal strain folding, pure shear folding, flexural flow folding and slip folding. Determining the relative importance of these models during folding is a fundamental problem for structural geologists, and has been the subject of numerous theoretical and field-based studies that seek to find criteria that discriminate between them (e.g. Lan and Hudleston, 1991; Davis, 1995; Hudleston et al., 1996; Bell and Hickey, 1997). Inclusion trail and fold geometries offer a means of distinguishing between the different models (e.g. Williams and Jiang, 1999), as each of the four fold mechanisms produces a different geometric relationship between limb rotation and inclusion trail curvature in sub-spherical porphyroblasts (Fig. 1). Tangential–longitudinal strain folds form by a bodily rotation, or spin, of the fold limbs, and all strain within a folded layer is coaxially accumulated. Porphyroblasts do not rotate relative to the folded layer, and rotate by $\leq$90° relative to the axial plane of the developing fold (Fig. 1b). Slip folding produces similar-type folds by simple shear parallel to the axial plane of the fold and potentially produces unlimited rotation of porphyroblasts relative to fold limbs and axial planes as limb rotation approaches 90° (Fig. 1c). During flexural flow, rotation of porphyroblasts relative to fold limbs is a response to vorticity induced by simple shear, and this rotation is opposite to that resulting from body rotation of the fold limbs (Fig. 1d). Pure shear folds result from passive amplification of pre-existing deflections by homogeneous coaxial flow and result in porphyroblast rotation relative to fold limbs only (Fig. 1e). Each of these fold models produces different amounts of porphyroblast rotation, relative to fold limbs and axial planes, for a given limb rotation. In real rocks, the amount of syn-folding porphyroblast rotation relative to fold limbs can be determined from inclusion trail curvature for all porphyroblasts that grew synchronous with, or after (in the case of a pre-existing porphyroblast) the fold event.

* Corresponding author. Current address: Institute of Geosciences, Shizuoka University, Shizuoka 422-8529, Japan. Tel.: +81-54-237-1111; fax: +81-54-238-0491.

E-mail address: aaron@se-geomail.sci.shizuoka.ac.jp (A. Stallard).

[1] Current address: Mineral Deposit Research Unit, Department of Earth and Ocean Sciences, University of British Columbia, Vancouver, BC, Canada V6T 1Z4.

0191-8141/01/$ - see front matter © 2001 Elsevier Science Ltd. All rights reserved.
PII: S0191-8141(01)00032-3

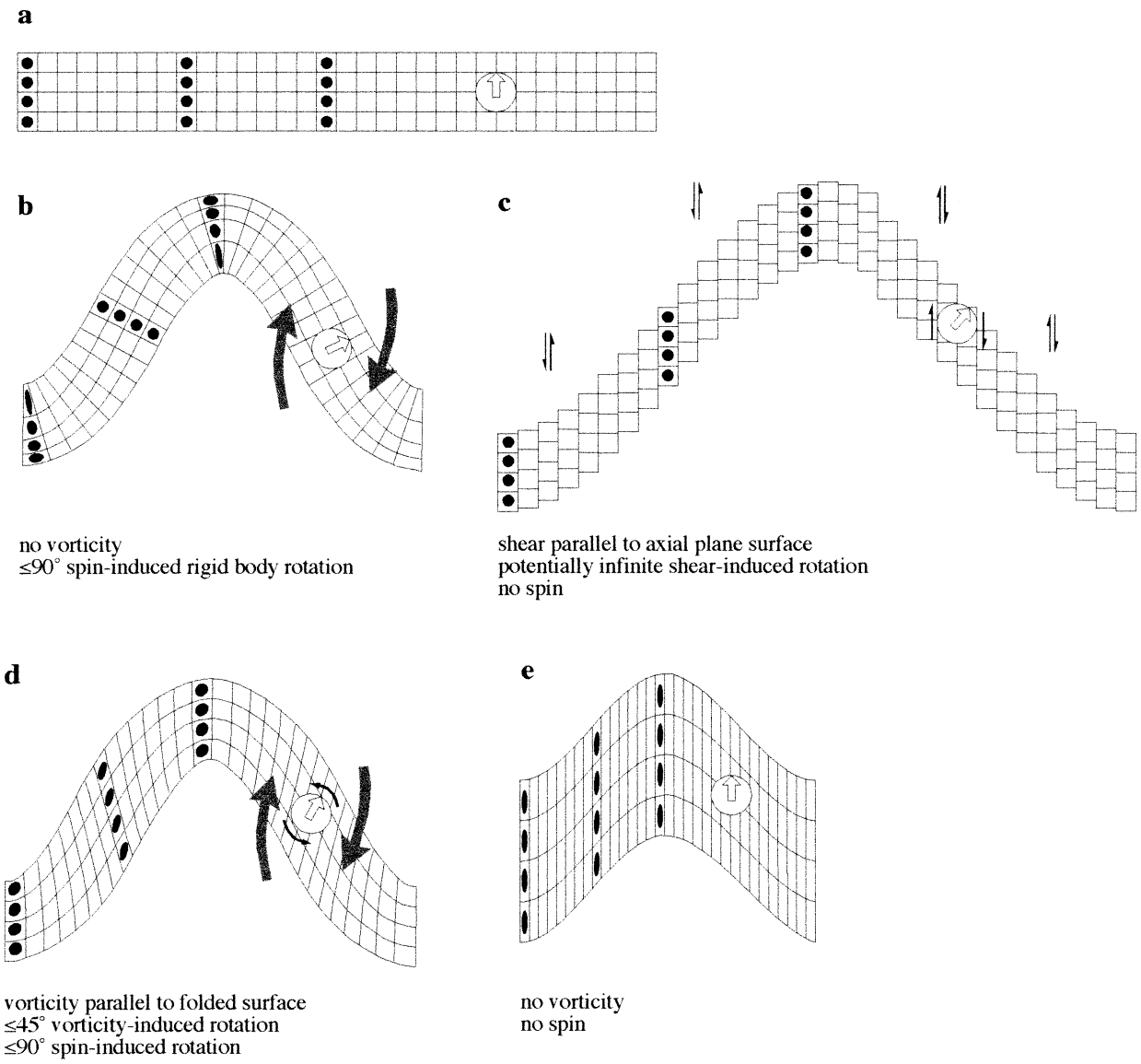

Fig. 1. Contrasting effects of four end-member fold mechanisms on porphyroblast rotation during folding. Vorticity refers to the amount of rotation that a flow type possesses, and spin refers to bodily rotation of the fold limbs in an external reference frame (see Passchier and Trouw, 1996). (a) Pre-deformation grid with strain markers (black circles) and porphyroblast (white circle). (b) In tangential longitudinal strain, porphyroblasts are rotated by an amount equivalent to the spin of fold limbs. (c) During slip folding, shear parallel to the axial plane of the fold produces potentially unlimited rotation of porphyroblasts as limb rotation approaches 90°. (d) In flexural flow, vorticity-induced rotation of porphyroblasts (large arrows) is opposite to rotation due to spin of the fold limbs (small arrows). Examples shown assume uniform vorticity distribution across all layers. (e) Pure shear folding involves homogeneous coaxial shortening with no rotation of porphyroblasts relative to geographic coordinates. Note that this example requires an initial folding of the pre-deformation grid by a mechanism other than pure shear. All four models as shown assume plane strain (i.e. no strain in the third dimension).

Rotation relative to axial planes, or geographic coordinates, is more difficult to evaluate and is usually assessed by the degree of variation of inclusion trail geometries across deformed terrains (e.g. Johnson, 1990; Busa and Gray, 1992; Bell et al., 1998; Kraus and Williams, 1998; Jung et al., 1999). If inclusion trail and fold geometries can be quantified, then the unique relationship between folding and extent of porphyroblast rotation specific to each fold model can be used to constrain the fold mechanisms that operated during deformation.

The Canton Schist, Georgia, USA, contains abundant garnet porphyroblasts with spiral inclusion trails, and records multiple fold events (Table 1). The three-dimensional (3-D) geometry of inclusion trails has been measured and described in detail by Stallard and Hickey (2001), who identified three fold events within the Canton Schist based upon these data (Table 1). The aim of this study is to use the inclusion trail and fold geometry data to constrain the fold mechanisms, and more specifically the contribution of flexural flow, during deformation of the Canton Schist. Different fold models are tested as suitable mechanisms to explain the measured inclusion trail and fold geometries,

Table 1
Previous published structural interpretations of the Canton Schist. The studies of McConnell and Abrams (1984) and German (1988, 1989) were of the Greater Atlanta area and Dahlonega gold belt respectively. The Canton Schist is located within both of these areas of study

McConnell and Abrams (1984)		German (1988, 1989)		Stallard and Hickey (2001)	
	Not recognised		Not recognised	S_1	Earliest foliation preserved within garnet cores only
F_1	Isoclinical recumbent ENE trending folds; dominant S-surface	F_1	Rootless recumbent isoclinal folds	F_2	Recumbent ENE trending folds
		S_1	NE trending foliation	S_2	Recognised within porphyroblasts and matrix
F_2	Upright to overturned, isoclinal to open NE trending folds. Responsible for outcrop patterns	F_2	Upright to NW vergent isoclinal to open NE trending folds	F_3	Upright E-W and NE trending folds
		S_2	Axial planar foliation. Locally transposes S1, responsible for most outcrop patterns	S_3	Axial planar foliation. Dominant matrix foliation
F_{2a}	Upright open NE trending folds	F_3	Upright open NNE trending folds. Responsible for some outcrop patterns		??
				F_4	NE trending recumbent folds
				S_4	Shallow dipping incipient matrix foliation
F_3	Open to isoclinal SW vergent SE trending folds. Mainly restricted to Blue Ridge		Not recognised		??
F_4	Upright open NW trending folds	F_4	Broad upright NNW trending folds		Not recognised

and the relationship between key parameters of folding and porphyroblast rotation are discussed.

2. Geological setting

The Canton Schist is part of the New Georgia Group, which is bound by two major northeast trending faults; the Allatoona Fault to the northwest and the Chattahoochee Fault to the southeast (see fig. 1 of Stallard and Hickey, 2001). The Allatoona Fault separates the New Georgia Group from biotite to kyanite grade metasedimentary rocks of the Ocoee Supergroup, whereas the Chattahooche Fault separates the New Georgia Group from higher grade migmatitic rocks of the Sandy Springs Group. The Canton Schist itself is a garnet–quartz–mica schist with a penetrative north–east striking schistosity. This schistosity is folded and locally crenulated, with incipient development of an axial plane foliation. Remnants of an earlier foliation are preserved adjacent to porphyroblasts and as crenulations in microlithons within the matrix (Stallard and Hickey, 2001). The dominant matrix foliation is sub-parallel to the axial planes of matrix crenulations and micro- and meso-scale isoclinal folds outlined by quartz veins (Fig. 2). Garnet porphyroblasts range from 4 to 8 mm in diameter, are sub-spherical and contain complex inclusion trail geometries. The inclusion trails within the cores commonly outline a simple sigmoidal geometry, but some porphyroblasts contain differentiated crenulated cleavages (Stallard and Hickey, 2001). Most garnets record $>90°$ rotation relative to the matrix, having spiral, rather than sigmoidal, inclusion trail geometries and inclusion trails are generally continuous from the core to the rim of porphyroblasts and into the matrix. More detailed descriptions of the regional geology and Canton Schist samples are available in Stallard and Hickey (2001).

3. Inclusion trail geometries and history of folding

The 3-D geometry of inclusion trails in garnet porphyroblasts from the Canton Schist have been measured and described in detail by Stallard and Hickey (2001). The inclusion trail geometries were constrained by measuring the pitch of sub-linear portions of inclusion trails from every garnet porphyroblast in each of over 400 oriented thin sections cut from 25 samples. Based upon the inclusion trail data and matrix structures, Stallard and Hickey

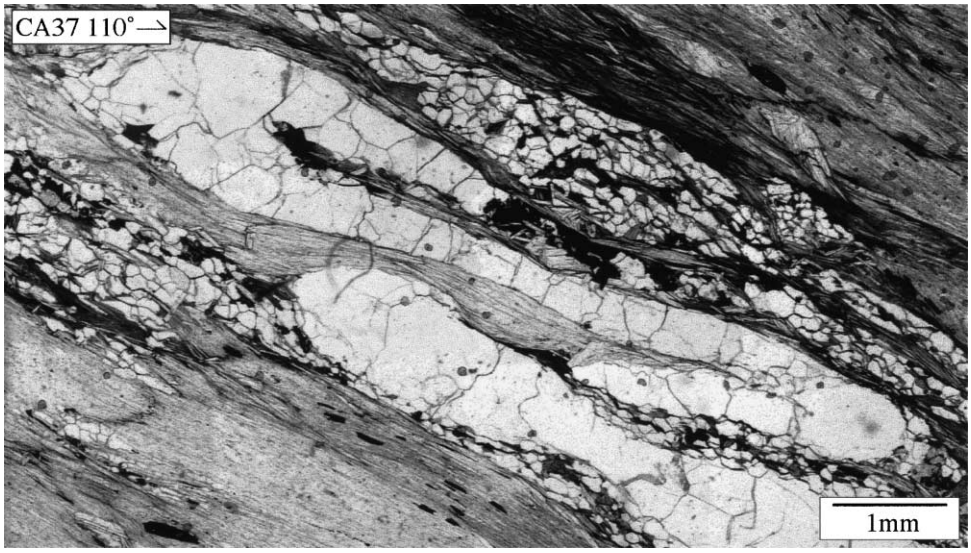

Fig. 2. Photomicrograph of isoclinal folded quartz vein. Vertical thin section, sample number and strike of section shown in top left corner.

proposed a model of folding and foliation development in the Canton Schist that involved three fold events (F_2–F_4) and four foliations (S_1–S_4; see fig. 12 of Stallard and Hickey, 2001). Three sub-planar inclusion trail surfaces (S_1–S_3) are recorded from the core to the rim of individual porphyroblasts, and these surfaces represent foliations that developed during the three overprinting fold events (Table 2). The earliest fold event is termed F_2, rather than F_1, because S_1 is the surface folded during this fold event, and S_2 is the axial plane foliation. The dominant matrix foliation is interpreted to be the folded equivalent of the S_3 inclusion trail foliation. This is based upon the consistent relationship between S_3-matrix curvature asymmetry and the orientation of the matrix foliation, and the observation that the inclusion

Table 2
Orientation of S_1–S_3 and matrix foliation from Canton Schist samples. The orientations of S_1–S_3 were determined from pitch measurements in oriented samples (see fig. 8 of Stallard and Hickey, 2001). Also shown are the angles between successive foliations in each sample. DipDr = dip direction, n = number of pitch measurements, sd = standard deviation. Data are from Stallard and Hickey (2001)

	S_1				S_2				S_3				Matrix		Angles between surfaces		
Sample	DipDr	Dip	n	sd	DipDr	Dip	n	sd	DipDr	Dip	n	sd	DipDr	Dip	S_1–S_2	S_2–S_3	S_3–Matrix
CA1	7	83	17	12.6	333	9	12	11.8	306	86	19	12.2	131	50	76	81	52
CA2	321	62	65	13.1	212	9	46	11.5	337	86	44	10.6	333	61	65	83	25
CA3	169	84	19	20.1	220	65	15	16.1	217	69	16	15.5	155	46	54	5	56
CA4	13	47	24	14.8	47	7	61	13.5	26	87	39	13.2	332	48	41	80	62
CA5	197	83	21	9.3	289	12	21	10.7	203	86	24	7.6	150	52	84	85	59
CA6	301	49	36	17.5	235	79	44	14.6	352	86	14	8.8	165	69	62	68	25
CA7	157	42	21	19	169	9	28	12.4	207	90	31	15.3	157	52	33	83	60
CA9	160	74	21	19.3	74	11	13	7.1	175	80	19	8.6	125	59	74	82	51
CA14	54	67	32	19.3	3	44	22	12	220	89	31	13.7	150	55	47	57	73
CA17a	134	54	25	17.7	115	8	8	11.5	324	83	16	14.3	138	60	46	90	37
CA19	91	85	27	11.4									150	75			
CA20	98	81	15	11.3									153	46			
CA23	32	88	25	8.6									136	60			
CA29	161	45	16	18.4	86	11	12	7.3	174	88	22	13	310	45	43	88	61
CA30	154	52	52	14.4	186	24	13	13.7	15	76	36	14	150	52	33	80	67
CA31	150	39	13	13.4	129	18	18	12.9	203	87	23	9.4	150	45	23	82	62
CA37	187	64	10	16.7	205	12	8	7.4	213	86	16	13.6	160	49	53	74	60
GA13	333	79	18	14.3	326	62	10	10.6	26	54	21	11.9	100	35	18	50	52
GA14	92	29	23	16.8	357	19	25	14.3	179	79	34	10.7	150	50	36	82	39
W1	178	21	13	15.3	165	44	19	16.9	360	70	19	13.1	330	40	24	67	38
W2a	211	64	12	11.6									330	60			
W2c	343	13	18	15.1	102	36	32	12.6	348	79	26	9.2	330	45	44	85	37
W2e	192	57	24	17.9	86	52	13	17					160	40	66		
W2f	67	64	25	13.9	36	43	33	15	198	76	50	15.6	154	52	32	63	46
Average			**23.8**	**15.1**			**22.7**	**12.4**			**26.3**	**12.1**					

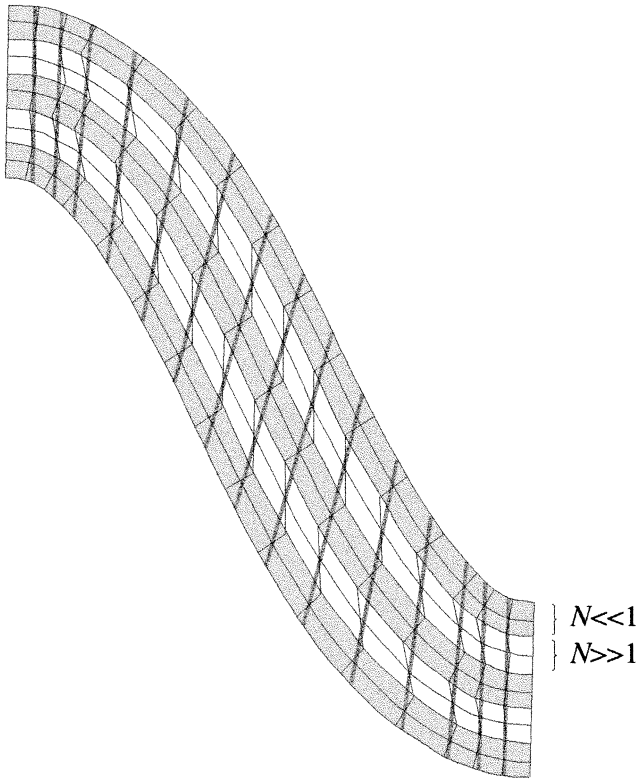

Fig. 3. Sketch showing variations in vorticity between folded layers within a sequence of alternating competent layers (grey) and soft layers (white). The parameter N describes the layer-parallel shearing within a layer as a multiple of the average shearing for the fold limb (Jiang, 1994). Shearing is concentrated in the softer layers ($N > 1$). Thin black lines indicate deflection of markers originally perpendicular to layering, according to finite-element model results of Hudleston et al. (1996). Thick grey lines are predicted deflections of markers for flexural flow in a rheological homogenous layer. Modified from Hudleston et al. (1996).

Table 3
Key to symbols and abbreviations used in the text

Ω_1^G	Porphyroblast rotation relative to the fold limb, measured in degrees
Ω_2^G	Porphyroblast rotation relative to the axial plane of developing folds, measured in degrees (see text for full description of reference frames used in this study)
Φ	Limb rotation
FF	Flexural flow folding
PS	Pure shear folding
FFΦ	Flexural flow component of limb rotation
FFΩ_1^G	Flexural flow component of porphyroblast rotation relative to fold limb
FFΩ_2^G	Flexural flow component of porphyroblast rotation relative to axial plane
PSΦ	Pure shear component of limb rotation
PSΩ_1^G	Pure shear component of porphyroblast rotation relative to fold limb
PSΩ_2^G	Pure shear component of porphyroblast rotation relative to axial plane
N	Layer-parallel shearing accommodated in a layer divided by the bulk shearing imposed by the deformation
Z	Ratio of $\sum\Omega_1^G$ to $\sum\Phi$ (i.e. $Z = \sum\Omega_1^G/\sum\Phi$)

trails in the garnet rims are commonly continuous with the matrix foliation (Stallard and Hickey, 2001). S_4 is an incipient foliation parallel to F_4 axial planes and is developed in the matrix and adjacent to porphyroblasts.

4. Testing fold mechanisms

In this section, the geometric relationship between inclusion trail and fold geometries is used to constrain the fold mechanisms, or combinations of fold mechanisms, that operated during deformation in the Canton Schist. In the following text, porphyroblast rotation during folding is described relative to two different reference frames, in the same manner as Williams and Jiang (1999): rotation relative to the fold limb (Ω_1^G), which is important as a measure of inclusion trail curvature, and rotation relative to the axial plane of developing folds (Ω_2^G), which is a measure of syn-folding porphyroblast rotation relative to geographic coordinates at the scale of the fold (i.e. minus the effects of bulk rotations of the rock mass at a scale larger than the fold). In this study, the term 'geographic coordinates' is also defined at the scale of the fold, and thus is independent of any large-scale rotation of the rock mass. Different fold mechanisms produce different amounts of Ω_1^G and Ω_2^G for a given amount of limb rotation (Fig. 1). Variation in vorticity between layers of contrasting competence also affects the amount of porphyroblast rotation, and is described by the parameter N (Jiang, 1994). N represents the layer-parallel shearing accommodated in a layer divided by the bulk shearing imposed by the deformation (Fig. 3). A list of all symbols and abbreviations used in the following sections is shown in Table 3.

4.1. Initial constraints

Fig. 4a shows values of limb rotation (Φ) and Ω_1^G during the F_3 and F_4 fold events in the Canton Schist. Calculations were not made for F_2, as the timing of porphyroblast nucleation relative to folding cannot be constrained, and therefore Ω_1^G is unknown. In contrast, during F_3 and F_4 porphyroblasts were present prior to folding. Values of Φ and Ω_1^G were calculated within the framework of the folding history described above (see also fig. 12 of Stallard and Hickey, 2001). For F_3, Φ cannot be determined exactly, but is estimated at close to 90°, as suggested by the near-orthogonal relationship between the S_2 and S_3 inclusion trail surfaces (Table 2), and the large amount of limb rotation required to generate 90° of inclusion trail curvature during a single fold event (Williams and Jiang, 1999). Given that the S_2 and S_3 surfaces probably represent the axial plane foliations rather than the fold limbs, $F_3\Phi$ may actually be less than 90°. The implications of this for the accuracy of the calculations is discussed later in the text. F_3 Ω_1^G is calculated from the angle between the S_2 and S_3 inclusion trail surfaces (Table 2). For F_4, Φ is calculated from the angle between the matrix foliation, which is the folded surface, and the average S_3

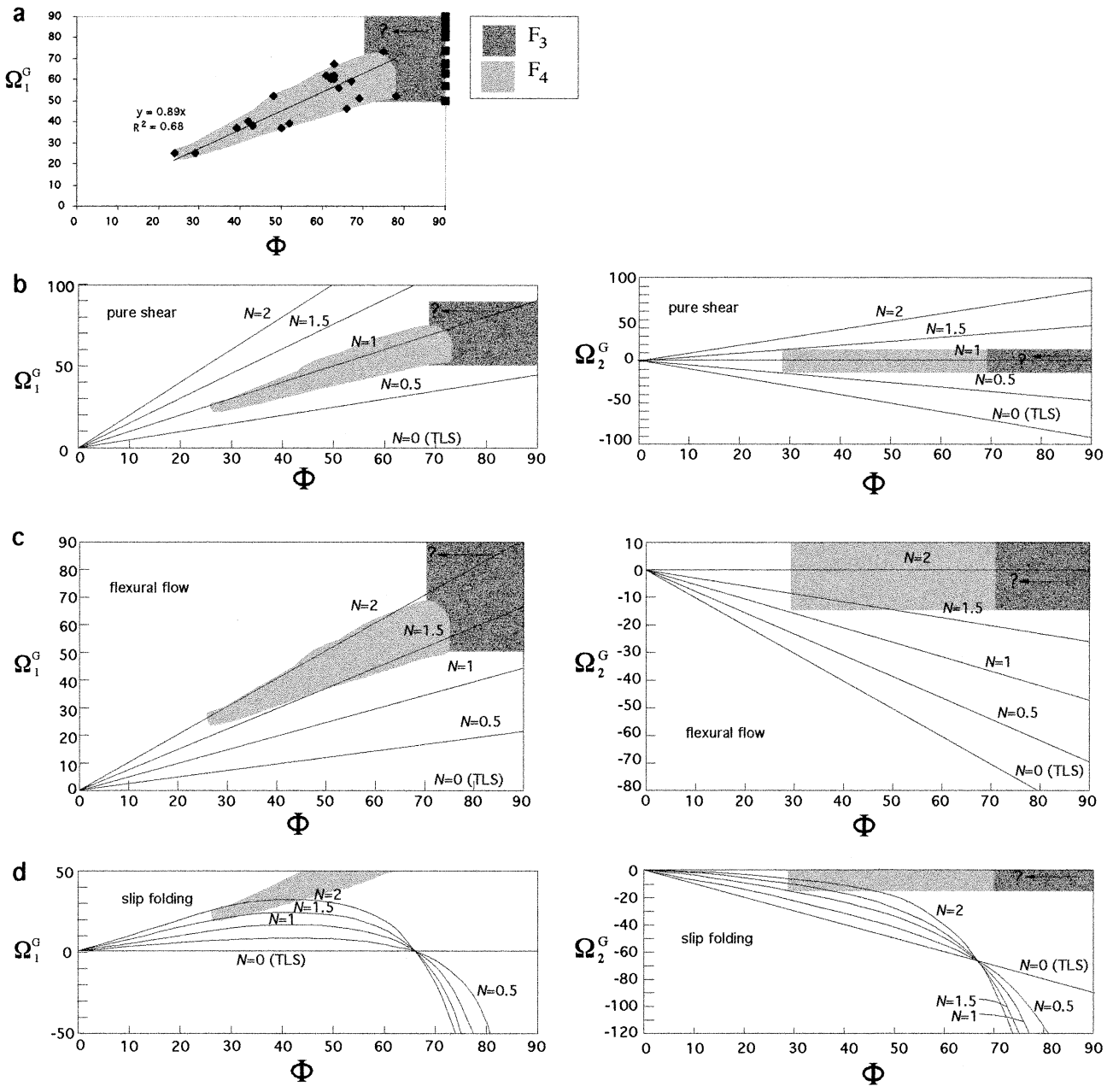

Fig. 4. (a) Amounts of fold limb rotation (Φ) and garnet rotation relative to fold limbs (Ω_1^G) measured from samples of Canton Schist. (b, c, d) The Canton Schist data shown in (a) has been transferred onto plots of the predicted patterns of porphyroblast rotation relative to fold limbs (Ω_1^G) and fold axial planes (Ω_2^G) for different values of limb dip (Φ) and rheological anisotropy (N) in each of the four end-member fold mechanisms. Note that tangential longitudinal strain folding (TLS) is represented by the $N = 0$ curves in any of the graphs. The degree of similarity of the Canton Schist data (grey areas) and predicted patterns (lines) indicates the ability of each fold mechanism to produce the observed geometries. Base graphs originally published by Williams and Jiang (1999).

orientation in porphyroblast rims, which represents the pre-folding orientation of the matrix foliation. Ω_1^G is calculated in essentially the same manner, from the angle between S_3 preserved in porphyroblast rims and the matrix foliation recorded from each sample (Table 2). In terms of estimating Ω_2^G, the inclusion trail data suggests Ω_2^G is minimal during folding (Stallard and Hickey, 2001), in agreement with theoretical predictions of Williams and Jiang (1999) that porphyroblasts affected by vorticity during folding will rotate little with respect to geographic coordinates. Accordingly, Ω_2^G is shown in Fig. 4 at $\leq 15°$. More detailed estimates of Ω_2^G, derived from fold and inclusion trail geometries, are discussed later in the text.

Fig. 4b–d shows the geometric relationships between Φ, N and the porphyroblast rotation produced by each of the four end-member fold mechanisms. All calculations assume perfect coupling between porphyroblasts and matrix. Values of Φ, Ω_1^G and Ω_2^G calculated for the Canton Schist (i.e.

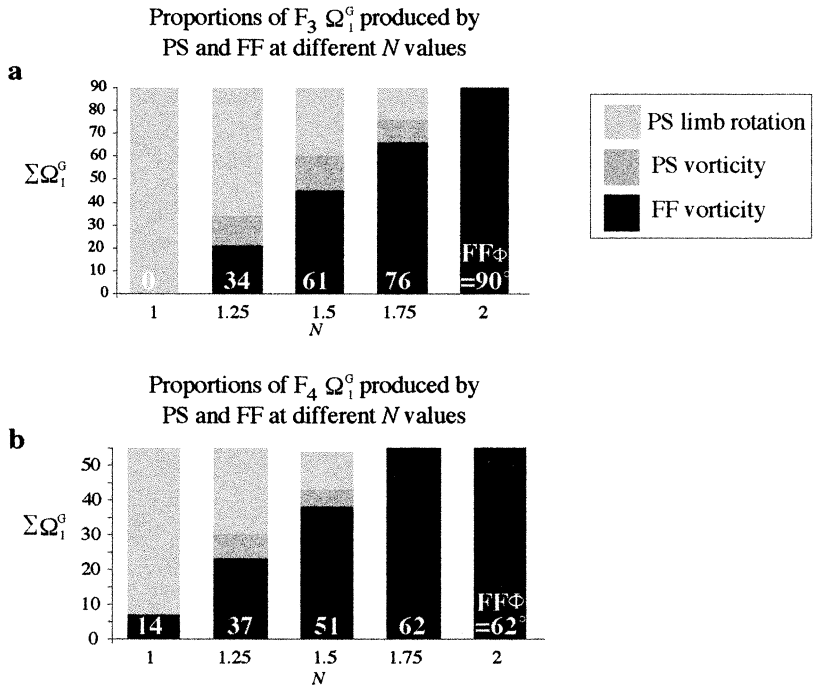

Fig. 5. Solution combinations of flexural flow and pure shear (that maximise flexural flow) that are consistent with the inclusion trail curvatures measured in the Canton Schist. Solutions are given for folding during F_3 (a) and F_4 (b) at different values of N. The amount of limb rotation in the flexural flow component of folding is displayed on the vertical bars. Note that a component of non-coaxial limb rotation occurs in pure shear when $N \neq 1$ (indicated by mid-grey shading).

shaded areas in Fig. 4a, as well as $\Omega_2^G \leq 15°$) are shown on these graphs to test the ability of each of the four fold models to generate the recorded geometries. From Fig. 4 it is apparent that only pure shear and flexural flow are capable of producing the fold and inclusion trail geometries measured in the Canton Schist (compare Fig. 4b and c with d). Tangential-longitudinal strain folding, represented by the $N = 0$ curves in Fig. 4, does not generate vorticity adjacent to porphyroblasts, so is unable to produce the measured Ω_1^G. Slip folding is also an unsuitable mechanism to explain the inclusion trail curvatures, as it does not accommodate shortening normal to axial planes, requires extreme anisotropy or isoclinal folds to generate $\Omega_1^G > 20°$, and produces large amounts of porphyroblast rotation relative to geographic coordinates (Fig. 4d), which is inconsistent with observed fold and inclusion trail data (Fig. 4a). However, flexural flow and pure shear are both capable of producing the observed geometries at approximately $N \approx 1.75$ and $N \approx 1$, respectively. During homogeneous pure shear (Fig. 4b, $N = 1$), the matrix is folded around the (non-rotating) porphyroblast and produces $\Omega_2^G = 0$. However, inhomogeneous pure shear ($N \neq 1$) produces a component of vorticity resembling flexural flow, and results in $\Omega_2^G \neq 0$ (Fig. 4b). Flexural flow produces both spin and vorticity components of porphyroblast rotation (Fig. 4c).

4.2. Maximum flexural flow component of folding

It is apparent from Fig. 4 that both pure shear and flexural flow, or some combination of both, are consistent with the geometric data. The relative proportions of flexural flow and pure shear that could have been active during folding in the Canton Schist can be constrained by using the inclusion trail and fold geometries to calculate the maximum possible flexural flow component of folding during F_3 and F_4. The component of flexural flow can be quantitatively expressed by either the amount of limb rotation by flexural flow (FFΦ), or the angular component of Ω_1^G due to vorticity in flexural flow ($FF\Omega_1^G$), as these variables have a positive linear relationship at constant N (Fig. 4c). Fig. 5 shows maximum possible values of $FF\Omega_1^G$ and FFΦ, at different values of N, during the F_3 and F_4 fold events. These values were calculated graphically from the relationships shown in Fig. 4, and the full set of results are given in Appendix A. The method of determining the values shown in Fig. 5 is as follows. Values of Ω_1^G and Ω_2^G for various combinations of PSΦ and FFΦ were calculated graphically from the plots in Fig. 4b and c. Those combinations of PSΦ and FFΦ that produce values of Ω_1^G and Ω_2^G similar to those measured in the Canton Schist are then potentially valid solutions. Of the possible solutions shown in Appendix A, those with the largest component of flexural flow are shown in Fig. 5. For solutions that involve components of both pure shear and flexural flow, pure shear was calculated after flexural flow, as is generally considered to be the case in the folding of natural rocks (e.g. De Sitter, 1958; Ramsay, 1962; Williams and Jiang, 1999). F_3 calculations were based upon $\Phi = 90°$ and $\Omega_1^G = 90°$, and for F_4, $\Phi = 62°$ and $\Omega_1^G = 55°$. These values were chosen because they

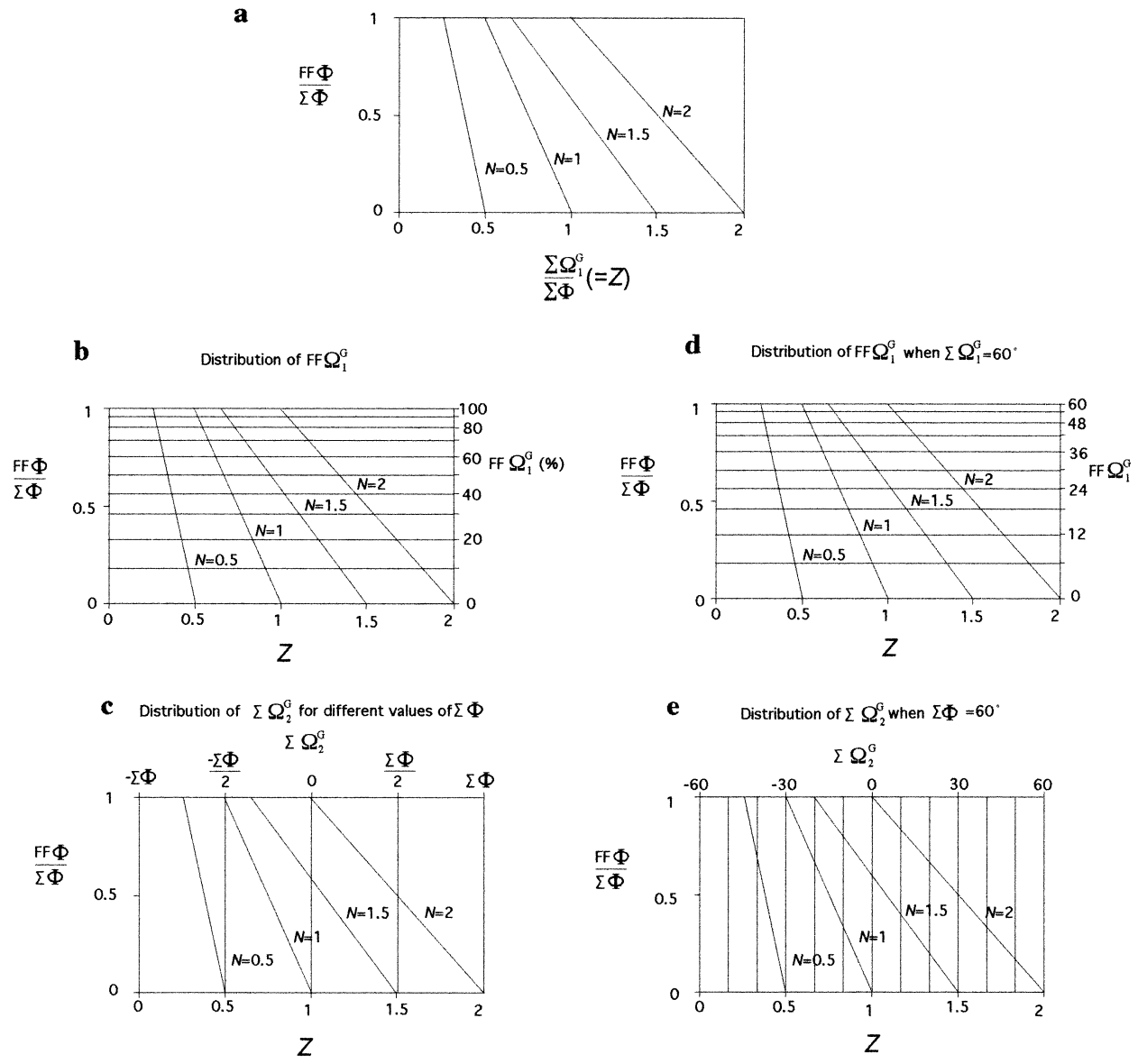

Fig. 6. Graphs showing the relationships between key variables that describe syn-folding porphyroblast rotation. The relationships shown in these graphs are true for any fold event that involves components of flexural flow and pure shear. (a) Relationship between Z, FFΦ and N. Calculation of this relationship is shown in Appendix B. The flexural flow component of total limb dip is constrained by the parameter Z, which describes the ratio of total rotation relative to fold limb ($\sum \Omega_1^G$), to total limb dip ($\Sigma\Phi$). This relationship is shown for different N values. The relationships of these parameters to total inclusion trail curvature generated by rotation in flexural flow (FFΩ_1^G (%)) is shown in (b). The amount of total porphyroblast rotation relative to the axial planes of the developing folds ($\sum \Omega_2^G$) is shown in (c). The values of FFΩ_1^G (b) and $\sum \Omega_2^G$ (c) vary with total limb dip, and are thus shown as percent and ratio of Φ, respectively. Examples of graphs (b) and (c) with designated values of total limb dip are shown in (d) and (e), respectively.

represent concentrations of Φ and Ω_1^G values measured in the Canton Schist (see Fig. 4a). As mentioned earlier, the values of $F_3\Phi$ are difficult to determine, and the effect on different $F_3\Phi$ values on the calculations are considered later in the text. A second set of F_4 calculations were made for $\Phi = 39°$ and $\Omega_1^G = 35°$ (Appendix A), which represents the smaller cluster of points shown on Fig. 4a. The calculations for $\Phi = 39°$ and $\Omega_1^G = 35°$ produce identical proportions of flexural flow as calculations for $\Phi = 62°$ and $\Omega_1^G = 55°$, indicating that the relative proportions of flexural flow and pure shear in the solutions shown in Fig. 5 are the same for any fixed ratio of Φ and Ω_1^G.

Three important trends emerged from the calculations:

1. The flexural flow component of folding is maximised with increasing N. Thus, the value of N in sampled layers must be determined before the true component of flexural flow folding can be calculated.
2. The limiting factor on the maximum possible FFΩ_1^G during each fold event, within the constraints of Φ and Ω_1^G shown in Fig. 4a, proved to be the ratio of $\sum \Omega_1^G$ to Φ (this ratio is herein termed the parameter Z). When $N \approx 1$, flexural flow produces $Z \approx 0.5$ (Fig. 4c), so inclusion trail curvatures recording $\Omega_1^G \approx 90°$, and

a

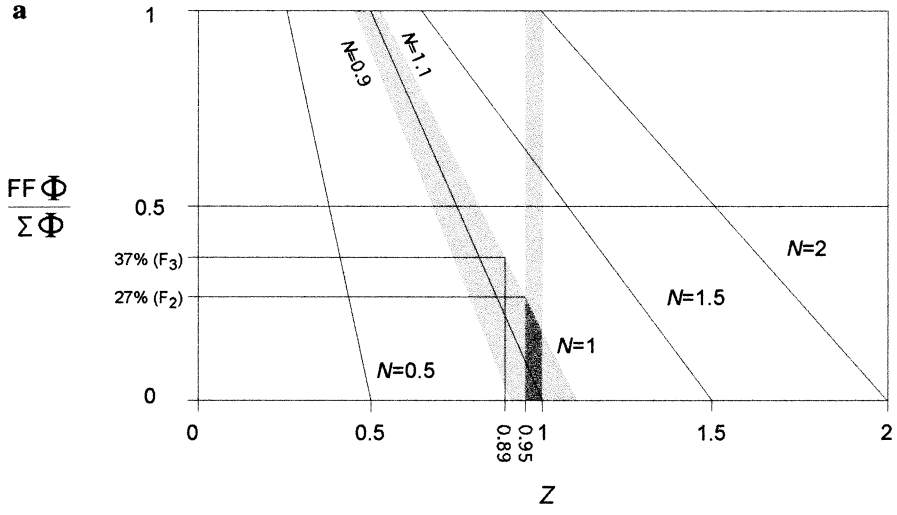

b

	Z	N	FFΦ	PSΦ	ΣΦ	FFΩ$_1^G$	PSΩ$_1^G$	ΣΩ$_1^G$	FFΩ$_2^G$	PSΩ$_2^G$	ΣΩ$_2^G$
F_3	0.95-1	0.9<*N*<1.1	24°	66°	90°	13°	72°	85°	-11°	6°	-5°
F_4	0.89	0.9<*N*<1.1	24°	41°	65°	13°	44°	57°	-11°	3°	-8°

Fig. 7. (a) Summary figure showing maximum possible flexural flow component of limb rotation during F_3 and F_4. The light grey areas represent the constraints of N (for both fold events) and Z (for F_3 only; the vertical line from $Z = 0.89$ is the Z value for F_4). The dark grey shading indicates the solution area for F_3, and the solution area for F_4 is that part of the vertical line at $Z = 0.89$ that intersects with the $0.9 \leq N \leq 1.1$ area. The maximum component of flexural flow limb dip within the solution areas is shown on the y-axis. (b) Summary of folding and rotation determined for each fold event in the Canton Schist. These values represent the maximum possible flexural flow component of folding within the constraints of the fold and inclusion trail geometries, and within the constraints of N. The total inclusion trail curvature produced by vorticity is highlighted in the light grey circles (for flexural flow and inhomogeneous pure shear) and the total rotation relative to fold axial planes (≈ geographic coordinates) is highlighted in the dark grey squares.

hence $Z \approx 1$, can only be explained by flexural flow if $N \approx 2$. Thus, any fold-porphyroblast system with $Z \approx 1$ and $N \approx 1$ involves little or no flexural flow.

3. All calculations of maximum flexural flow during the two fold events produce $\sum \Omega_2^G < 10°$ (Appendix A), indicating minimal syn-folding net rotation of porphyroblasts relative to geographic coordinates. These values of $\sum \Omega_2^G$ reflect the constraints of the values of Z for the samples, and *are not limited* by values of $\sum \Omega_2^G$ estimated earlier from the patterns of measured inclusion trail pitches (i.e., $\sum \Omega_2^G$ earlier estimated at ≤15°, see Fig. 4b–d).

It is apparent that Z and N are the most important parameters in this method of determining fold mechanisms that operated during deformation. Accordingly, the relationships between Z, N and other parameters of folding and rotation are determined below. Following this, values of N are estimated for the Canton Schist and used to constrain maximum $FF\Omega_1^G$.

4.2.1. Z and other parameters of folding and rotation

The relationship between Z, maximum FFΦ and N is displayed graphically in Fig. 6a. These relationships are valid for folding that involves components of pure shear and flexural flow, and were determined by solving FFΦ in terms of Z for different N (see Appendix B for full calculations). From these calculations, the following relationship was determined:

$$\frac{FF\Phi}{\sum \Phi} = 2 - \frac{2Z}{N} \tag{1}$$

and this relationship is shown in Fig. 6a. The relationships of $FF\Omega_1^G$ (inclusion trail curvature resulting from vorticity-induced rotation of porphyroblast during flexural flow) and $\sum \Omega_2^G$ (total rotation of porphyroblasts relative to fold axial planes) to Z, N and FFΦ have been determined in a similar way and are shown graphically in Fig. 6b and c, respectively. In both figures, the relationships are overlain on the graph shown in Fig. 6a. Calculations are presented in Appendix B, and yield the following relationships.

For any value of N

$$\frac{FF\Omega_1^G}{\sum \Omega_1^G} = \frac{FF\Phi}{2\sum \Phi - FF\Phi} \tag{2}$$

(this relationship is shown in Fig. 6b) and

$$\sum \Omega_2^G = \sum \Phi(Z - 1) \tag{3}$$

(this relationship is shown in Fig. 6c).

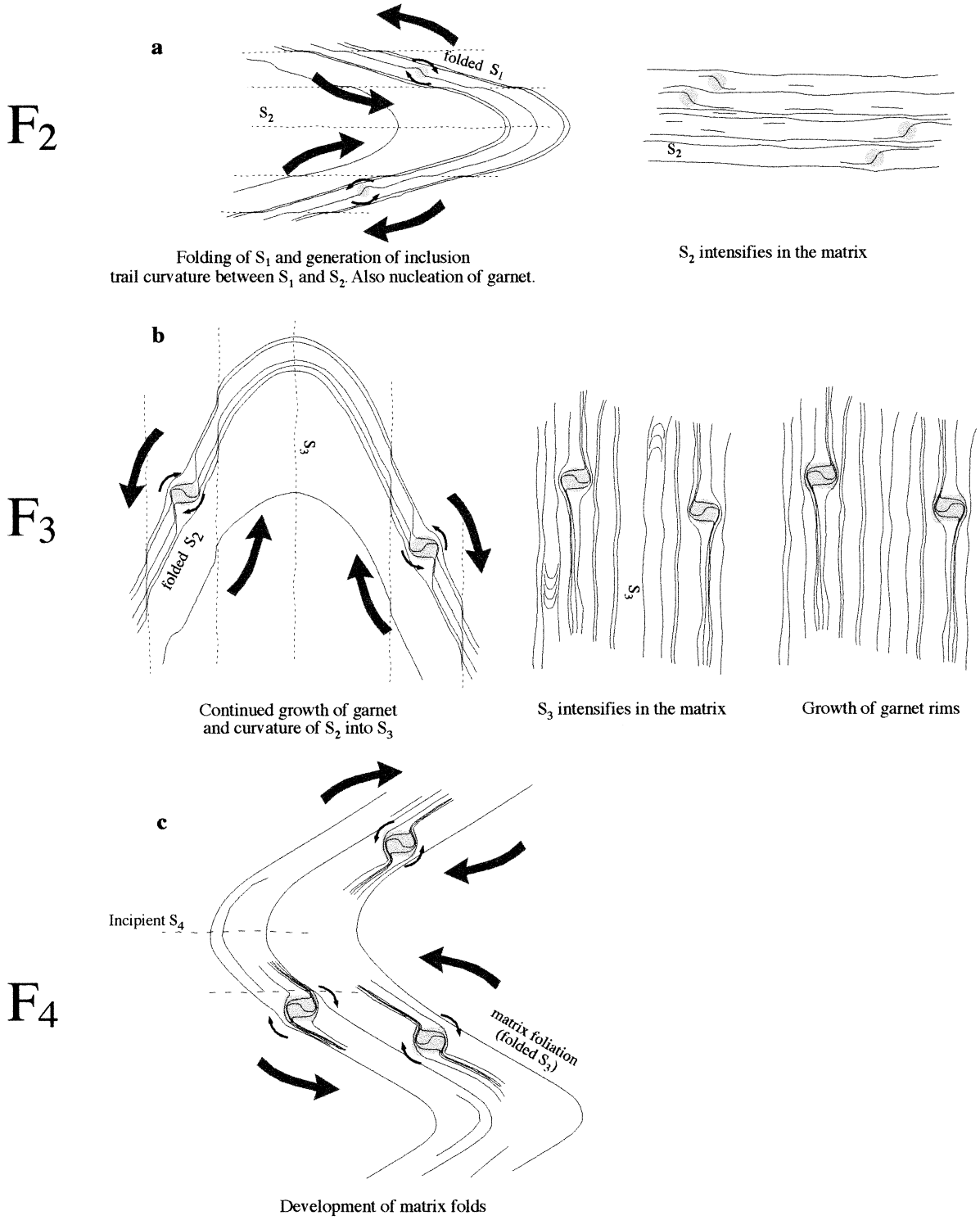

Fig. 8. Schematic model showing the development of inclusion trails in the Canton Schist in terms of flexural flow folding and porphyroblast rotation. The large grey arrows indicate spin of the fold limbs, which produces rotation of the porphyroblats relative to the axial planes. The smaller black arrows indicate vorticity, or rotation of the porphyroblast with respect to the fold limbs. In this model, rotation of porphyroblasts due to spin is approximately equal to that due to vorticity (i.e. $N \approx 2$). This results in minimal net rotation of the porphyroblasts, as suggested by the Canton Schist data (Fig. 7b). View is parallel to the fold axes, or rotation axes for each fold event. Note that the three porphyroblasts shown in **c** have the same spiral axes, but different inclusion trail geometries and asymmetries. Such patterns are present in the inclusion trail data (Stallard and Hickey, 2001) and reflect the position of the porphyroblast relative to fold hinges during each of the fold events.

The graphs in Fig. 6 describe the relationships between the different parameters that define porphyroblast rotation during folding. These parameters are limb rotation (Φ), variation in vorticity between layers (N), rotation relative to fold limbs (Ω_1^G), rotation relative to the fold axial plane (Ω_2^G), and the maximum flexural flow component of folding (FFΦ). The relationships shown in Fig. 6 have some important implications for determining the proportions of flexural flow and pure shear folding in a flexural flow–pure shear fold model such as that proposed here for the Canton Schist. For example, once Z and N are constrained for a given fold or fold event, it is then possible to determine: (i) the proportions of limb rotation resulting from flexural flow and from pure shear (Fig. 6a), (ii) the amounts of porphyroblast rotation relative to fold limbs produced by flexural flow and by pure shear (Fig. 6b), and (iii) the total amount of porphyroblast rotation relative to axial planes (Fig. 6c). Note that the amount of rotation relative to the fold axial plane is constant for a value of Z independent of N (Fig. 6c). This last observation means that rotation relative to axial planes can be determined once the value of Z is known, and remains valid independent of the value of N and the proportions of flexural flow and pure shear folding. The above relationships offer a means of determining fold mechanisms and net porphyroblast rotation in other folded terrains where the parameters Z and N can be determined.

Within the Canton Schist, the two measured inclusion trail curvatures have Z ratios of 0.89 (F_4 curvature) and ≈ 1 (F_3 curvature), as shown in Fig. 4a. These values indicate minimal rotation of the porphyroblast relative to axial planes of developing folds (Fig. 6c). The value of N within the Canton Schist is more difficult to constrain, and is considered below before a final estimate of the maximum flexural flow component of folding can be made.

4.2.2. Constraints on the value of N

The flexural flow component of folding is maximised when N is between 1.75 and 2 (Fig. 5). Such values of N describe a layered rock mass made up of alternating competent and incompetent rheologies (e.g. Fig. 3; Hudleston et al., 1996; Williams and Jiang, 1999). This type of layering is not evident in the Canton Schist, and the following evidence suggests $N \approx 1$ during folding in the Canton Schist. All the samples collected for this study are of similar texture, mineralogy and structure. Schistose layering in outcrop ranges from a continuous schistosity with no discernible layering, to alternating quartz-rich and mica-rich domains of between $\approx 100\ \mu m$ and several mm thickness. These domains anastomose and are commonly discontinuous on the scale of a thin section. Garnet porphyroblasts have comparable microstructures in all samples and all layers within the rock mass, are larger than the scale of schistose layering, and occur in samples with both continuous and layered schistosities. To produce large N values by rheological variations at a scale larger than the Canton Schist requires that adjacent rock units be involved in the folding, and have a higher competence (lower N) than the Canton Schist. This is difficult to assess, as the timing of folding relative to movements on the Allatoona and Chattahoochee Faults (see fig. 1 of Stallard and Hickey, 2001) is unknown. Given the uniformity of schistosity and consistency in inclusion trail patterns in all samples, N is assumed to be close to one, and a maximum of $N = 1.1$ has been used in further calculations.

4.2.3. Final estimates of the flexural flow component of folding in the Canton Schist

Fig. 7 shows the solution field of the maximum possible flexural flow component of folding (grey areas on plot in Fig. 7a), within a flexural flow–pure shear system, during F_3 and F_4 within the constraints of Z and N determined above. The results are summarised numerically in Fig. 7b. The parameters Z and N were found to be the limiting factors on maximising FFΩ_1^G. Syn-folding garnet rotation relative to axial planes is $\leq 8°$ for both F_3 and F_4 solutions. During F_3 and F_4, folding involved a maximum of 24° limb rotation by flexural flow. During F_3, flexural flow produced $\leq 27\%$ limb rotation, and during F_4, $\leq 37\%$, with the remainder produced by pure shear. Inclusion trail curvature, which represents the relative rotation of porphyroblasts and fold limbs during folding, is largely due to rotation of fold limbs relative to (irrotational) garnet porphyroblasts, with $\leq 22\%$ of curvature during F_3 and $\leq 28\%$ of curvature during F_4 produced by vorticity-induced rotation of porphyroblasts relative to (irrotational) fold limbs. These are the maximum values possible in a folding history of flexural flow followed by pure shear in which flexural flow is maximised.

These results depend upon accurate estimates of N and Z. It is possible that the actual values vary from those in Fig. 7. For instance, $F_3\Phi$ may be less than the estimated 85–90° (see above). A smaller $F_3\Phi$ results in a larger Z value, and this effectively reduces the flexural flow component of folding within the constraints of $N < 1.1$ shown in Fig. 7a. Also, if N is greater than that estimated, then the maximum possible flexural flow component of folding also increases (Figs. 5 and 7). Estimates of Z are more easily determined for F_4 than F_3, as both S_3 (pre-folding orientation) and the matrix foliation (post-folding orientation) are easily identified and measured in all samples.

5. Discussion

5.1. Implications for fold mechanisms in schistose rocks

Although spiral inclusion trails may appear smoothly curving, detailed mapping of inclusion trails has revealed that inclusion trail curvature commonly occurs in approximately 90° increments (e.g. Hayward, 1990; Bell et al., 1992; Johnson, 1992). For spirals that formed in fold environments, this suggests inclusion trail curvature accumulated over multiple fold events at approximately 90°

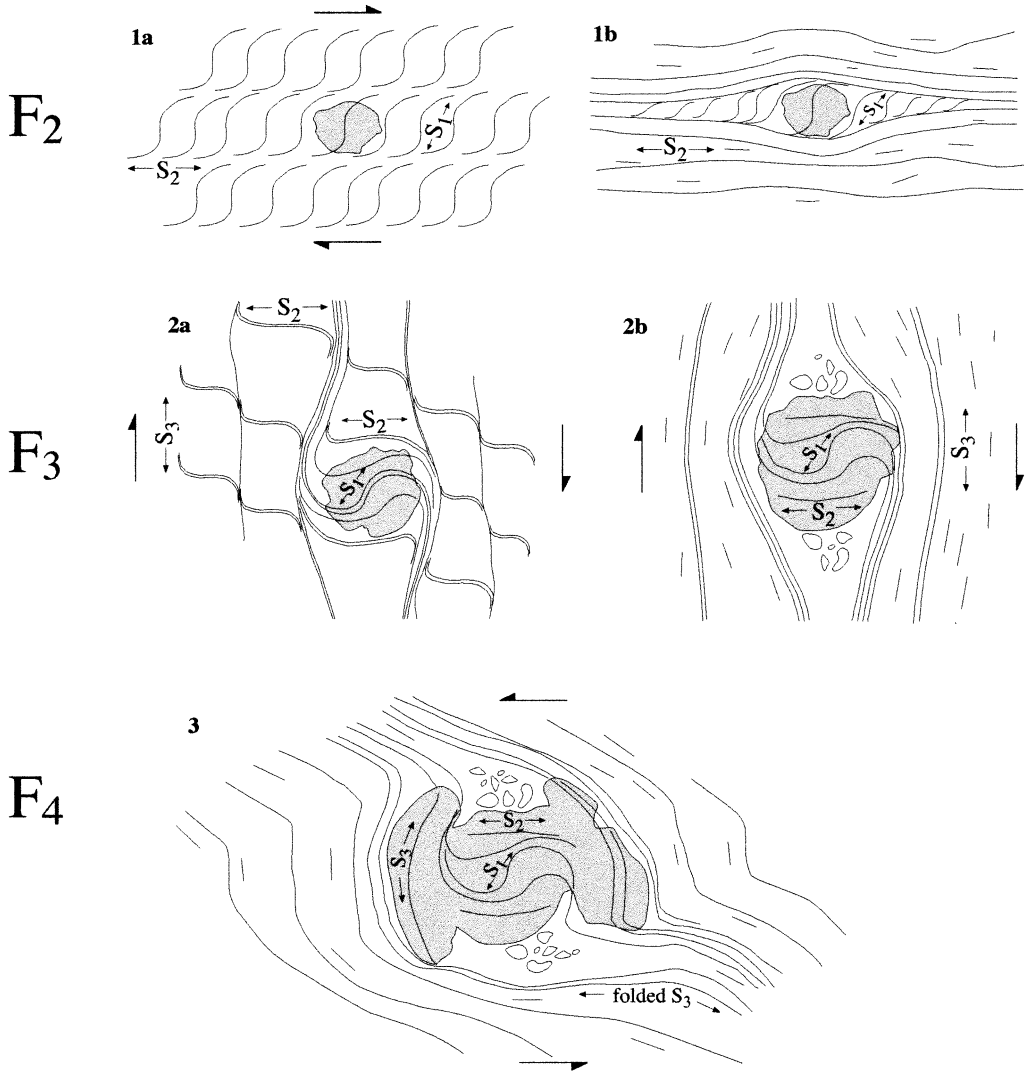

Fig. 9. Schematic model showing the development of inclusion trails in the Canton Schist in terms of pure shear folding and porphyroblast non-rotation. Note that the deformation is partly non-coaxial, as occurs when $N \neq 1$. This model also approximates deformation predicted in the PBIS model. (1a and 1b) S_1 is crenulated during folding (F_2) and development of S_2. Garnet porphyroblasts nucleate during F_2 and preserve S_1 as curved inclusion trails. (2a) A third foliation (S_3) develops during F_3, accompanied by crenulation of S_2. Porphyroblasts grow over S_2. (2b) Final development of S_3. S_1 and S_2 have been destroyed in the matrix, but are preserved within the porphyroblast. (3) S_3 is folded in the matrix.

curvature per fold event. Such large amounts of curvature produce Z values close to one, and thus minimal net porphyroblast rotation (Fig. 6c) and minimal flexural flow folding for $N = 1$ (Fig. 6a). Given these conditions, significant amounts of flexural flow requires $N > 1.5$ and hence strongly layered rocks with contrasting competencies between adjacent layers and concentration of vorticity in certain layers. The alternative is minor flexural flow and large amounts of pure shear, or other fold processes that produce approximately 90° inclusion trail curvature without porphyroblast rotation.

There are several theoretical problems with accommodating a large component of folding by pure shear. These include the amount of strain required to rotate fold limbs in pure shear, and the fact that pure shear folding involves essentially homogeneous deformation when rocks are rheologically heterogeneous and deformation is also generally observed to be heterogeneous in space and time (e.g. Passchier and Trouw, 1996). Conventional models of pure shear folding, such as that shown in Fig. 1, generally depict conditions of plane strain and relatively homogeneous deformation in individual layers. This type of model is simplified and may be inadequate to explain fold deformation without consideration of additional processes. For example, folding in schistose rocks by bulk pure shear may also involve: (i) partitioning of strain into domains of shortening and zones of shortening plus shearing (e.g. Bell 1986), (ii) shear at a low angle to the fold axial plane (e.g. Mamtani et al., 1999), and (iii) reactivation of pre-existing heterogeneities such as bedding and schistosities (e.g. Davis, 1995). Inclusion of these factors into fold models may produce solutions more consistent with the geometries

of natural folds and related structures such as foliations and inclusion trails.

An example of a fold model that incorporates such complications is the progressive bulk inhomogeneous shortening (PBIS) model (Bell, 1981, 1985; Bell and Hickey, 1997). PBIS is a geometrical model similar to the shear folding model of Ramsay (1967) and the clay brick model of De Sitter (1958), while accommodating shortening normal to bulk shortening, volume loss during cleavage development, and shear strain at a low angle to the fold axial plane. Bulk coaxial deformation is partitioned into anastomosing zones of noncoaxial progressive shearing strain and volume loss, and zones of coaxial progressive shortening (Bell, 1981; Bell and Hickey, 1997). Folding during PBIS involves bulk coaxial deformation and formation of an anastomosing foliation subparallel to the axial plane. With progressive deformation, zones within the rock become non-coaxial and accommodate shear at a low angle to S_1. In the PBIS model, deformation does not involve flexural shear, as layering is modelled as being mechanically inactive. The model also predicts that porphyroblasts will not rotate within the zones of progressive shortening provided they do not deform internally.

In terms of the Canton Schist data, PBIS is an alternative model that can explain the measured inclusion trail geometries by overprinting foliations developed during successive fold events. However, the matrix folds which generated curvature between S_3 and the matrix foliation formed with only incipient development of an axial plane cleavage. This may be because folding occurred by reactivation of S_3. Reactivation of bedding and early foliations oblique to fold axial planes is predicted to occur when zones of progressive shearing switch from anastomosing around the axial plane to anastomosing around earlier discordant foliations or bedding (Bell, 1985, 1986). These surfaces reactivate with a sense of shear that is antithetic relative to the fold. In the Canton Schist, the zones of progressive shearing may have anastomosed around the S_3 surface in the matrix to produce the matrix folds.

5.2. Models of flexural flow and pure shear folding in the Canton Schist

Folding in the Canton Schist probably involved a larger component of pure shear than of flexural flow (Fig. 7). The actual relative proportions of flexural flow and pure shear depend upon the value of N in the sampled layers. If $N \approx 2$, then the maximum possible component of flexural flow is 100% (Fig. 5), whereas when $N \approx 1$, the maximum component is $<15\%$. As discussed above, N is probably ≈ 1 in the Canton Schist, but theoretically, the measured inclusion trail geometries can be produced by either flexural flow or pure shear folding, a combination of both, or an alternative mechanism such as PBIS. Flexural flow folding produces porphyroblast rotation from the spin of the fold limbs and vorticity parallel to the folded layer (Fig. 1). The spin and vorticity components of rotation have opposing senses of rotation (Fig. 1d). As N approaches two, the vorticity-induced component of rotation approaches the spin-induced component of porphyroblast rotation, and thus results in minimal *net* rotation of the porphyroblast relative to geographic coordinates (Fig. 4c). In this way, it is possible to produce the measured inclusion trail geometries in the Canton Schist by flexural flow. Fig. 8 shows such a model of fold and inclusion trail development in the Canton Schist. By contrast, a model of pure shear folding involves folding about a non-rotating porphyroblast, although it must be noted that pure shear in rocks of $N \neq 1$ results in a degree of non-coaxial deformation (Fig. 4b). Such a folding model produces a similar relationship between inclusion trails and folds to that predicted in the PBIS model, and this is shown in Fig. 9. The model in Fig. 9 is consistent with the observed inclusion trail geometries in the Canton Schist, although at $N \approx 1$ (cf. $N \approx 2$ for flexural flow model). Note that similar inclusion trail geometries can result from the two models shown in Figs. 8 and 9.

6. Conclusions

1. The important parameters that describe the relationships between fold mechanisms and inclusion trail curvature in a pure shear-flexural flow deformation are Z (the ratio between the total porphyroblast rotation relative to fold limbs, and the total limb rotation) and N (the variation in vorticity between different layers within the rock mass). Once Z and N are determined for a specific fold event, it is then possible to calculate: (i) the proportions of limb rotation resulting from flexural flow and from pure shear, (ii) the amounts of porphyroblast rotation relative to fold limbs produced by flexural flow and by pure shear, and (iii) the total amount of porphyroblast rotation relative to axial planes.
2. Combinations of flexural flow and pure shear were tested to explain the measured fold and inclusion trail geometries produced during F_3 and F_4 in the Canton Schist. During F_3 and F_4, flexural flow produced a maximum of $\leq 27\%$ and $\leq 37\%$ of measured limb rotation, respectively, which corresponds to a maximum of 24° limb rotation by flexural flow in each fold event. The remainder of limb rotation resulted from deformation in pure shear. The maximum possible component of flexural flow increases with increasing N. Alternative fold mechanisms that partition non-coaxial deformation around porphyroblasts may also have been active during folding.
3. Inclusion trail curvature within the Canton Schist, which represents the relative rotation of porphyroblasts and fold limbs during folding, is largely due to rotation of fold limbs relative to (irrotational) garnet porphyroblasts. A maximum of only $\leq 22\%$ of curvature during F_3 and $\leq 28\%$ of curvature during F_4 could have been produced

by rotation of porphyroblasts relative to (irrotational) fold limbs.

4. The maximum estimated syn-folding rotation of garnet porphyroblasts relative to geographic coordinates is $\approx 5°$ during F_3 and $\approx 8°$ during F_4.

Acknowledgements

We thank Tim Bell, Paul Williams, Roger Gibson, Andy Barker, and Peter Hudleston for their critical assessments of earlier manuscript versions. Gerry German and Tim La Tour provided helpful advice on Southern Appalachian geology, and Dazhi Jiang is acknowledged for fruitful discussion on concepts contained within this paper. Constructive reviews by Scott Johnson and Manish Mamtani greatly improved the manuscript. This research was supported by a James Cook University Merit Research Award, and the principal author acknowledges the support of a JSPS Fellowship at Shizuoka University during the final stages of manuscript preparation.

Appendix A

A.1. Calculation of the maximum flexural flow component of folding during F_3 and F_4 in the Canton Schist

The following tables show the amount of Ω_1^G and Ω_2^G produced by various combinations of flexural flow and pure shear folding at varying *N*. Calculations were made graphically from relationship shown in Fig. 4.

F_3 fold event: Bold numbers indicate solutions that maximise the component of flexural flow at *N* values of 1, 1.25, 1.5, 1.75, and 2, and are consistent with values of Ω_1^G and Φ measured from F_3 in the Canton Schist. These results are shown graphically in Fig. 5a.

F_4 fold event: Calculations were made determine the maximum component of flexural flow folding during F_3 for $\Omega_1^G = 55$ and $\Phi = 62$ (a), and $\Omega_1^G = 35$ and $\Phi = 39$ (b).

Bold numbers indicate solutions that maximize the component of flexural flow at *N* values of 1, 1.25, 1.5, 1.75, and 2, and are consistent with values of Ω_1^G and Φ measured from F_4 in the Canton Schist. These results are shown graphically in Fig. 5b.

Appendix B

B.1. Calculation of relationship between key variables of syn-folding porphyroblast rotation

The following calculations were performed to determine the relationships between the variables *N*, *Z*, FFΦ, $FF\Omega_1^G$ and $\sum \Omega_2^G$. The results of the calculations are shown graphically in Fig. 6. Fig. 6a shows the relationship between FFΦ, *N* and *Z*, Fig. 6b describes the relationship between

F_3 calculations

	Flexural flow component of folding			Pure shear component of folding			Total folding		
n	Ω_1^G	Ω_2^G	Φ	Ω_1^G	Ω_2^G	Φ	Ω_1^G	Ω_2^G	Φ
1	**0**	**0**	**0**	**90**	**0**	**90**	**90**	**0**	**90**
1.25	0	0	0	52	10	42	52	10	42
1.25	8	− 5	12	78	15	62	80	10	74
1.25	11	− 7	18	88	17	71	99	10	89
1.25	15	− 10	25	50	10	40	65	0	65
1.25	18	− 12.5	30	60	12.5	50	78	0	80
1.25	**21**	**− 14**	**34**	**70**	**14**	**56**	**90**	**0**	**90**
1.25	15	− 10	24	0	0	0	15	− 10	24
1.25	21	− 13	34	69	13	56	90	0	90
1.25	30	− 20	48	52	10	42	80	− 10	90
1.5	25	− 10	33	32	10	22	59	0	56
1.5	25	− 10	34	63	20	42	88	10	76
1.5	31	− 12.5	43	70	22.5	47	100	10	90
1.5	38	− 15	52	48	15	33	86	0	85
1.5	37	− 15	50	17	5	11	54	− 10	61
1.5	40	− 16	55	50	16	35	90	0	87
1.5	**45**	**− 13**	**61**	**45**	**13**	**29**	**90**	**0**	**90**
1.75	0	0	0	25	10	14	25	10	14
1.75	30	− 5	35	40	15	22	70	10	57
1.75	33	− 5	38	12	5	6	45	0	44
1.75	54	− 9	63	48	19	27	102	10	90
1.75	60	− 10	69	0	0	0	60	− 10	69
1.75	66	− 11	76	24	11	14	90	0	90
1.75	**67**	**− 10**	**77**	**23**	**10**	**13**	**90**	**0**	**90**
2	80	0	80	20	10	10	100	10	90
2	**90**	**0**	**90**	**0**	**0**	**0**	**90**	**0**	**90**

F_4 calculations (App. A cont'd)

		Flexural flow component of folding			Pure shear component of folding			Total folding		
	n	Ω_1^G	Ω_2^G	Φ	Ω_1^G	Ω_2^G	Φ	Ω_1^G	Ω_2^G	Φ
a	**1**	**7**	**−7**	**14**	**48**	**0**	**48**	**55**	**−7**	**62**
	1.25	**23**	**−15**	**37**	**32**	**6**	**25**	**55**	**−9**	**62**
	1.5	**38**	**−15**	**51**	**17**	**5**	**11**	**55**	**−10**	**62**
	1.75	31	−5	35	47	9	27	78	−1	62
	1.75	49	−8	56	10	4	6	59	−4	62
	1.75	**55**	**−9**	**62**	**0**	**0**	**0**	**55**	**−9**	**62**
	2	62	0	62	0	0	0	62	0	62
b	**1**	**4**	**−4**	**8**	**31**	**0**	**31**	**35**	**−4**	**39**
	1.25	**16**	**−10**	**24**	**19**	**3**	**15**	**35**	**−7**	**39**
	1.5	25	−10	34	8	2	5	33	−8	39
	1.5	**23**	**−9**	**31**	**12**	**4**	**8**	**35**	**−5**	**39**
	1.75	**34**	**−5.5**	**38**	**0**	**0**	**0**	**34**	**−5.5**	**38**
	2	37	0	37	0	0	0	37	0	37

FFΦ, *N*, *Z* and $FF\Omega_1^G$ and Fig. 6c shows the relationship between FFΦ, *N*, *Z* and $\sum \Omega_2^G$.

Many of the initial relationships introduced in the following equations are derived from the plots in Fig. 4, which are in turned derived from Williams and Jiang (1999). For example, Eq. (B3) below expresses the total rotation of porphyroblasts relative to fold limbs, when $N = 1.5$, in terms of the amount of limb rotation in FF and in PS. These relationships are sourced from Fig. 4b and c, where it is shown that at $N = 1.5$, $FF\Omega_1^G = 3/4FF\Phi$, and $PS\Omega_1^G = 3/2\Phi$. The sum of these two components gives $\sum \Omega_1^G$, as shown in Eq. (B3) below.

1. Calculation of relationships shown in Fig. 6a. These calculations explore the relationship between FFΦ (expressed as $FF\Phi/\sum\Phi$), *N* and *Z*. The first two equations are introduced in the main text.

$$Z = \frac{\sum \Omega_1^G}{\sum \Phi} \tag{B1}$$

$$FF\Phi + PS\Phi = \sum \Phi \tag{B2}$$

(a) When $N = 1.5$,

$$\tfrac{3}{4}FF\Phi + \tfrac{3}{2}PS\Phi = \sum \Omega_1^G \tag{B3}$$

(derived from Fig. 4b and c)From Eq. (B2),

$$PS\Phi = \sum \Phi - FF\Phi \tag{B4}$$

Substitute Eq. (B4) into Eq (B3) gives:

$$FF\Phi = 2\sum \Phi - \tfrac{4}{3}\sum \Omega_1^G \tag{B5}$$

From Eq. (B1),

$$\sum \Omega_1^G = \sum \Phi Z \tag{B6}$$

Substitute Eq. (B6) into Eq. (B5) gives:

$$\frac{FF\Phi}{\sum \Phi} = 2 - \tfrac{4}{3}Z \tag{B7}$$

(b) When $N = 1$,

$$\tfrac{1}{2}FF\Phi + PS\Phi = \sum \Omega_1^G \tag{8}$$

(derived from Fig. 4b and c)Substitute Eq. (B4) into Eq. (B8) gives:

$$FF\Phi = 2\sum \Phi - 2\sum \Omega_1^G \tag{B9}$$

Substitute Eq. (B6) into Eq. (B9) gives:

$$\frac{FF\Phi}{\sum \Phi} = 2 - 2Z \tag{B10}$$

(c) When $N = 2$,

$$FF\Phi + 2PS\Phi = \sum \Omega_1^G \tag{B11}$$

(derived from Fig. 4b and c)Substitute Eq. (B4) into Eq. (B11) gives:

$$FF\Phi = 2\sum \Phi - \sum \Omega_1^G \tag{B12}$$

Substitute Eq. (B6) into Eq. (B12) gives:

$$\frac{FF\Phi}{\sum \Phi} = 2 - Z \tag{B13}$$

(d) When $N = 0.5$,

$$\tfrac{1}{4}FF\Phi + \tfrac{1}{2}PS\Phi = \sum \Omega_1^G \tag{B14}$$

(derived from Fig.4b and c)Substitute Eq. (B4)into Eq. (B14) gives:

$$FF\Phi = 2\sum \Phi - 4\sum \Omega_1^G \tag{B15}$$

Substitute Eq. (B6) into Eq. (B15) gives:

$$\frac{FF\Phi}{\sum \Phi} = 2 - 4Z \tag{B16}$$

The four calculations at different *N* values give the same

solution;

$$\frac{FF\Phi}{\sum\Phi} = 2 - \frac{2Z}{N}$$

and this is shown graphically in Fig. 6a.

2. Calculation of relationship shown in Fig. 6b. These calculations explore the relationship between FFΦ and $FF\Omega_1^G$ at different values of *N*.

(a) When $N = 1$,

$$\frac{FF\Omega_1^G}{\sum\Omega_1^G} = \frac{\frac{1}{2}FF\Phi}{\frac{1}{2}FF\Phi + PS\Phi} \quad (B17)$$

(derived from Fig. 4b and c)Substitute Eq. (B4) into Eq. (B17) gives,

$$\frac{FF\Omega_1^G}{\sum\Omega_1^G} = \frac{\frac{1}{2}FF\Phi}{\frac{1}{2}FF\Phi + \sum\Phi - FF\Phi}$$

(b) When $N = 2$,

$$\frac{FF\Omega_1^G}{\sum\Omega_1^G} = \frac{FF\Phi}{FF\Phi + 2PS\Phi} \quad (B18)$$

(derived from Fig. 4b and c)Substitute Eq. (B4) into Eq. (B18) gives,

$$\frac{FF\Omega_1^G}{\sum\Omega_1^G} = \frac{FF\Phi}{2\sum\Phi - FF\Phi}$$

(c) When $N = 0.5$,

$$\frac{FF\Omega_1^G}{\sum\Omega_1^G} = \frac{\frac{1}{4}FF\Phi}{\frac{1}{4}FF\Phi + \frac{1}{2}PS\Phi} \quad (B19)$$

(derived from Fig.4)Substitute Eq. (B4) into Eq. (B19) gives,

$$\frac{FF\Omega_1^G}{\sum\Omega_1^G} = \frac{FF\Phi}{2\sum\Phi - FF\Phi}$$

(d) When $N = 1.5$,

$$\frac{FF\Omega_1^G}{\sum\Omega_1^G} = \frac{\frac{3}{4}FF\Phi}{\frac{3}{4}FF\Phi + \frac{3}{2}PS\Phi} \quad (B20)$$

(derived from Fig. 4)Substitute Eq. (B4) into Eq. (B20) gives,

$$\frac{FF\Omega_1^G}{\sum\Omega_1^G} = \frac{FF\Phi}{2\sum\Phi - FF\Phi}$$

The four calculations at different *N* values give the same solution;

$$\frac{FF\Omega_1^G}{\sum\Omega_1^G} = \frac{FF\Phi}{2\sum\Phi - FF\Phi}$$

and this is shown graphically in Fig. 6b.*3. Calculation of relationships shown in Fig. 6c*. These calculations explore the relationship between $\sum\Omega_2^G$, FFΦ and *Z* at different values of *N*.

(a) When $N = 1.5$,

$$\sum\Omega_2^G = -\frac{1}{4}FF\Phi + \frac{1}{2}PS\Phi \quad (B21)$$

(from Fig. 4b and c)Substitute Eq. (B4) into Eq. (B21) gives

$$\sum\Omega_2^G = \frac{1}{2}\sum\Phi - \frac{3}{4}FF\Phi \quad (B22)$$

Substitute Eq. (B7) into Eq. (B22) gives

$$\sum\Omega_2^G = \sum\Phi(Z-1)$$

(b) When $N = 1$,

$$\sum\Omega_2^G = -\frac{1}{2}FF\Phi \quad (B23)$$

(derived from Fig. 4b and c)Substitute Eq. (B10) into Eq. (B23) gives

$$\sum\Omega_2^G = \sum\Phi(Z-1)$$

(c) When $N = 2$,

$$\sum\Omega_2^G = PS\Phi \quad (B24)$$

(derived from Fig. 4b and c)Substitute Eq. (B4) into Eq. (B24) gives

$$\sum\Omega_2^G = \sum\Phi - FF\Phi \quad (B25)$$

Substitute Eq. (B13) into Eq. (B25) gives

$$\sum\Omega_2^G = \sum\Phi(Z-1)$$

(d) When $N = 0.5$,

$$\sum\Omega_2^G = -\frac{3}{4}FF\Phi - \frac{1}{2}PS\Phi \quad (B26)$$

(from Fig. 4b and c)Substitute Eq. (B4) into Eq. (B26) gives

$$\sum\Omega_2^G = -\frac{1}{4}FF\Phi - \frac{1}{2}\sum\Phi \quad (B27)$$

Substitute Eq. (B16) into Eq. (B26) gives

$$\sum\Omega_2^G = \sum\Phi(Z-1)$$

The four calculations at different *N* values give the same solution;

$$\sum\Omega_2^G = \sum\Phi(Z-1)$$

and this is shown graphically in Fig. 6c.

References

Bell, T.H., 1981. Foliation development: the contribution, geometry and significance of progressive bulk inhomogeneous shortening. Tectonophysics 75, 273–296.

Bell, T.H., 1985. Deformation partitioning and porphyroblast rotation in metamorphic rocks: a radical reinterpretation. Journal of Metamorphic Geology 3, 109–118.

Bell, T.H., 1986. Foliation development and refraction in metamorphic rocks: reactivation of earlier foliations and decrenulation due to shifting patterns of deformation partitioning. Journal of Metamorphic Geology 4, 421–444.

Bell, T.H., Hickey, K.A., 1997. Distribution of pre-folding linear movement indicators around the Spring Hill Synform, Vermont: significance

for mechanism of folding in this portion of the Appalachians. Tectonophysics 274, 275–294.

Bell, T.H., Forde, A., Hayward, N., 1992. Do smoothly curving, spiral-shaped inclusion trails signify porphyroblast rotation. Geology 20, 59–62.

Bell, T.H., Hickey, K.A., Upton, G.J.G., 1998. Distinguishing and correlating multiple phases of metamorphism across a multiply deformed region using the axes of spiral, staircase and sigmoidally curved inclusion trails in garnet. Journal of Metamorphic Geology 16, 767–794.

Busa, M., Gray, N., 1992. Rotated staurolite porphyroblasts in the Littleton Schist at Bolton, Connecticut, USA. Journal of Metamorphic Geology 10, 627–636.

Davis, B.K., 1995. Regional-scale foliation reactivation and re-use during formation of a macroscopic fold in the Robertson River Metamorphics, north Queensland, Australia. Tectonophysics 242, 293–311.

De Sitter, L.U., 1958. Boudins and parasitic folds in relation to cleavage and folding. Geology en Mijnbouw 20, 277–286.

German, J.M., 1985. The geology of the northeastern portion of the Dahlonega gold belt, Georgia Geological Survey Bulletin 30, 190pp.

German, J.M., 1988. The geology of gold occurrences in the west-central Georgia Piedmont, Georgia Geological Survey Bulletin 107, 48pp.

Hayward, N., 1990. Determination of early fold axis orientations within multiply deformed rocks using porphyroblasts. Tectonophysics 179, 353–369.

Hudleston, P.J., Treagus, S.H., Lan, L., 1996. Flexural flow folding: does it occur in nature?. Geology 24, 203–206.

Jiang, D., 1994. Flow variation in layered rocks subjected to bulk flow of various kinematic vorticities: theory and geological implications. Journal of Structural Geology 16, 1159–1172.

Johnson, S.E., 1990. Lack of porphyroblast rotation in the Otago Schists, New Zealand: implications for crenulation cleavage development, folding and deformation partitioning. Journal of Metamorphic Geology 8, 13–30.

Johnson, S.E., 1992. Sequential porphyroblast growth during progressive deformation and low-P high-T metamorphism, Cooma Complex, Australia: the use of microstructural analysis to better understand deformation and metamorphic histories. Tectonophysics 214, 311–339.

Jung, W.-S., Ree, J.-H., Park, Y., 1999. Non-rotation of garnet porphyroblasts and 3-D inclusion trail data: an example from the Imjingang belt, South Korea. Tectonophysics 307, 381–395.

Kraus, J., Williams, P.F., 1998. Relationships between foliation development, porphyroblast growth and large-scale folding in a metaturbidite suite, Snow Lake, Canada. Journal of Structural Geology 20, 61–76.

Lan, L., Hudleston, P.J., 1991. Finite element models of buckle folds in non-linear materials. Tectonophysics 199, 1–12.

Mamtani, M.A., Karanth, R.V., Greiling, R.O., 1999. Are crenulation cleavage zones mylonites on the microscale?. Journal of Structural Geology 21, 711–718.

McConnell, K.I., Abrams, C.E., 1984. Geology of the Greater Atlanta Region, Georgia Geological Survey Bulletin 96, 127pp.

Passchier, C.W., Trouw, R.A.J., 1996. Microtectonics. Springer-Verlag, Berlin.

Ramsay, J.G., 1962. The geometry and mechanics of formation of 'similar' type folds. Journal of Geology 70, 309–327.

Ramsay, J.G., 1967. Folding and Fracturing of Rocks. McGraw-Hill, New York.

Stallard, A.R., Hickey, K.A., 2001. Shear zone vs folding origin for spiral inclusion trails in the Canton Schist. Journal of Structural Geology 23, 1845–1864.

Williams, P.F., Jiang, D., 1999. Rotating garnets. Journal of Metamorphic Geology 17, 367–378.